Journal of Theoretical Biology 256 (2009) 533–546

Contents lists available at ScienceDirect

Journal of Theoretical Biology

journal homepage: www.elsevier.com/locate/yjtbi

Mathematical modelling of fibre-enhanced perfusion inside a tissue-engineering bioreactor

Robert J. Whittaker [a,*], Richard Booth [a], Rosemary Dyson [b,c], Clare Bailey [d], Louise Parsons Chini [e], Shailesh Naire [f], Sevil Payvandi [g], Zimei Rong [h], Hannah Woollard [c], Linda J. Cummings [i], Sarah L. Waters [a], Lina Mawasse [j], Julian B. Chaudhuri [j], Marianne J. Ellis [j], Vipin Michael [k], Nicola J. Kuiper [k], Sarah Cartmell [k]

[a] Mathematical Institute, University of Oxford, OX1 3LB, UK
[b] Centre for Plant Integrative Biology, University of Nottingham, LE12 5RD, UK
[c] School of Mathematical Sciences, University of Nottingham, NG7 2RD, UK
[d] Department of Civil and Building Engineering, Loughborough University, LE11 3TU, UK
[e] Complex Systems Research Center, University of New Hampshire, NH 03824, USA
[f] School of Computing and Mathematics, University of Keele, ST5 5BG, UK
[g] Department of Bioengineering, Imperial College London, SW7 2AZ, UK
[h] Interdisciplinary Research Centre in Biomedical Materials, Queen Mary University of London, E1 4NS, UK
[i] Department of Mathematical Sciences, New Jersey Institute of Technology, University Heights, Newark, NJ 07102-1982, USA
[j] Department of Chemical Engineering, Centre for Regenerative Medicine, University of Bath, BA2 7AY, UK
[k] Institute of Science and Technology, University of Keele, ST4 7QB, UK

ARTICLE INFO

Article history:
Received 4 March 2008
Received in revised form
8 September 2008
Accepted 7 October 2008
Available online 25 October 2008

Keywords:
Tissue engineering
Bioreactor
Darcy flow
Mathematical modelling

ABSTRACT

We develop a simple mathematical model for forced flow of culture medium through a porous scaffold in a tissue-engineering bioreactor. Porous-walled hollow fibres penetrate the scaffold and act as additional sources of culture medium. The model, based on Darcy's law, is used to examine the nutrient and shear-stress distributions throughout the scaffold. We consider several configurations of fibres and inlet and outlet pipes. Compared with a numerical solution of the full Navier–Stokes equations within the complex scaffold geometry, the modelling approach is cheap, and does not require knowledge of the detailed microstructure of the particular scaffold being used. The potential of this approach is demonstrated through quantification of the effect the additional flow from the fibres has on the nutrient and shear-stress distribution.

1. Introduction

Currently, efforts to induce healing and regeneration of damaged adult cartilage and bone are being directed towards improving existing cell therapies and developing new tissue-engineering strategies. Small focal cartilage defects can be successfully treated with autologous cells (Peterson et al., 2000). Multiple and extensive defects require more complex osteochondral tissues, the successful engineering of which could potentially provide long-term benefit to a huge number of individuals. The general strategy for tissue engineering involves seeding cells onto a biomaterial scaffold and culturing the seeded scaffold in a bioreactor (Martin et al., 2004).

More complex osteochondral tissues require bilayered scaffolds and bespoke bioreactors. Furthermore they require close monitoring of the cells. For example, the cells require complex nutrition that includes oxygen, glucose, and ascorbate. Waste products, such as lactate and carbon dioxide, can build up locally. This lowers the pH of the surrounding culture medium, which can be harmful to the cells. In addition, bone (Rubin et al., 2006) and cartilage (Knobloch et al., 2008) are mechanosensitive tissues, and so it is critical for the developing tissue to receive appropriate mechanical stimuli.

A current challenge is the development of bespoke bioreactors that will overcome nutrient transport limitations and subject the cells to optimal dynamic compression. Current strategies take advantage of the scaffold morphology. Typically, the scaffolds are highly porous (70–90%), with pore diameters ranging from 250 to 600 μm. Perfusion bioreactors are used to force culture medium through the scaffold pores, enhancing nutrient transport and

* Corresponding author. Tel.: +44 1865 280618.
URL: http://robert.mathmos.net/ (R.J. Whittaker).

0022-5193/$ - see front matter © 2008 Elsevier Ltd. All rights reserved.
doi:10.1016/j.jtbi.2008.10.013

providing mechanical stimuli to the cells (e.g. Abousleiman and Sikavitsas, 2006; Cimetta et al., 2007; Kim et al., 2007). For small tissue-engineered constructs these methods have been shown to be successful in comparison to static culture (Glowacki et al., 1998; Goldstein et al., 2001; Bancroft et al., 2002; Cartmell et al., 2003). However, problems arise when the tissue size is scaled up. Cells residing away from the inlets and outlets may sit in almost stagnant regions, where both nutrient delivery and shear stress are compromised. If the centre of the construct is to receive adequate flow, then regions near the inlet and outlet may suffer by receiving too much shear stress. The non-uniformity of the flow and shear-stress distributions is problematic.

To address these issues, various new techniques are being developed. For example, degradable poly(lactic-co-glycolic acid) (PLGA) porous-walled fibres may be incorporated into the scaffold design. In addition to the standard perfusion of culture medium through the scaffold, additional culture medium is injected through the fibres. Cartmell et al. (2007) and Michael et al. (2007) describe a dual-chamber bioreactor, as shown in Fig. 1. In the larger bone section, one or two porous fibres pass though holes drilled in the scaffold from one side of the chamber to the other. As well as enhancing the distribution of culture medium, the fibres can act as conduits for sensor probes, which can provide data on nutrient levels. A typical porous hydroxyapatite scaffold is shown in Fig. 2A (Gittings et al., 2005). A cross-section through the wall of a typical porous fibre is shown in Fig. 2B (Ellis and Chaudhuri, 2007; Morgan et al., 2007).

One method of predicting the flow field and nutrient transport in bioreactor systems of this type is to use computational fluid dynamics (CFD) simulations (see, for example Porter et al., 2005; Boschetti et al., 2006). Such simulations can provide detailed solutions on the pore scale for a given system. However, they are computationally expensive, and require detailed knowledge of the pore-scale microstructure. In this paper, we show how simple mathematical modelling can be used as an alternative to experimental 'trial and error' and full CFD simulations, to allow the optimization of an experimental protocol for desired flow and nutrient transport properties. Our modelling approach does not require full details of the microstructure and can be applied to a wide variety of bioreactor systems.

Relatively few mathematical modelling studies have focused on bioreactor culture of cell-seeded porous constructs for tissue engineering (see MacArthur et al., 2004; O'Dea et al., 2008). While many studies consider reaction–diffusion type systems (e.g. Galban and Locke, 1997; Nehring et al., 1999) fewer consider reaction and transport by diffusion *and convection* within a polymer scaffold (e.g. Lasseux et al., 2004). Some models have been developed that integrate mechanical and chemical factors that control the functional development of tissue engineered constructs (Sengers et al., 2004; Lemon et al., 2006). However, these models do not account for coupling between the externally driven flow and the construct domains.

Several theoretical studies have investigated the external flow and nutrient fields *surrounding* a tissue construct in a bioreactor, in which the construct is modelled either as an impermeable solid (Galban and Locke, 1999; Humphrey, 2003; Cummings and Waters, 2007) or an impermeable fluid bag (Waters et al., 2006). These studies determine the shear stress experienced by, and the nutrient delivery to, the surface of the tissue construct; however, no account is taken of the processes occurring within the porous scaffold.

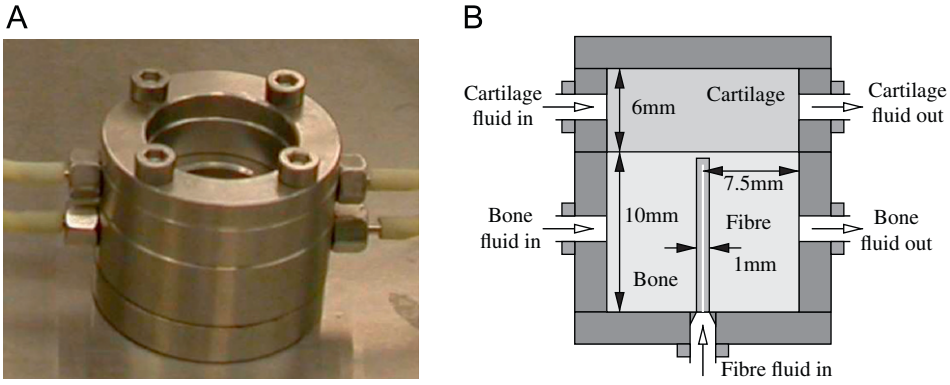

Fig. 1. A photograph (A) and sketch (B) of the two-chamber modular bioreactor, set up for configuration B (see Section 2). The tubes to the left and right provide flow to and from the inlet and outlet pipes, and porous fibre can be inserted through the base.

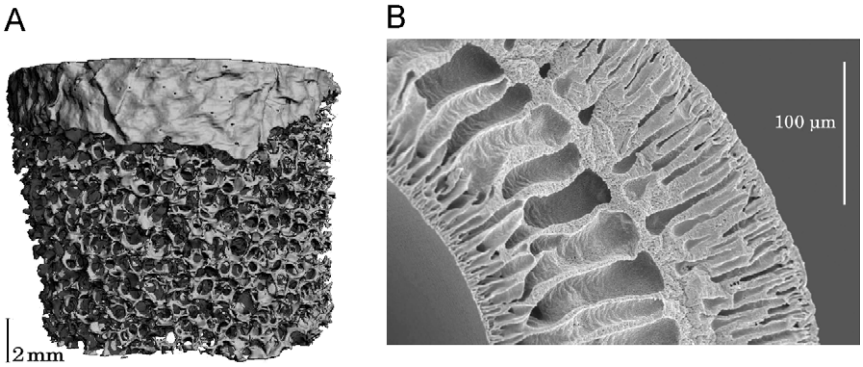

Fig. 2. (A) A MicroCT image of a capped porous hydroxyapatite scaffold, provided by Jon Gittings and Irene Turner at the University of Bath. (B) An SEM image of a transverse cross-section through the wall of one of the PLGA fibres, manufactured by Ellis and Chaudhuri. Typical dimensions for both constructs are given in Table 1.

In contrast to these studies, we investigate the role of fluid flow *within* the scaffold, including both externally driven flow and additional perfusion from the porous fibres. We consider two flow domains—the fibres and the space occupied by the scaffold around them—and couple the flows via continuity conditions at the interfaces. The scaffold is modelled as a uniform isotropic porous medium, with sources of fluid from inlet and outlet pipes, as well as the porous fibres. Within the fibres, a separate fluid-dynamical problem is solved to compute the outflow through the fibre walls. We exploit geometric features, such as the slender geometry of the fibres, to simplify the full Navier–Stokes equations, and enable analytical progress. The model results in a Poisson problem for the flow in the scaffold, which we solve numerically. It is therefore a much cheaper problem to solve than direct numerical simulation of the full Navier–Stokes equations within the complex scaffold geometry. Once the fluid flow is known, the distributions of shear stress, nutrients and waste products can be determined, along with the consequences for cell proliferation. We show the potential of this approach by providing example solutions to three bioreactor systems similar to those proposed by Cartmell et al. (2007). We pay particular attention to the effect of the additional flow from the porous fibres, and demonstrate the power of our modelling for making predictions of the optimal experimental protocol.

This paper is organized as follows. The bioreactor model is developed in Sections 2–4. Numerical solutions for the fluid flow throughout the porous scaffold are presented in Section 5 for three different fibre configurations. In Section 6, we examine the shear stress experienced by the growing cells, and in Section 7 the problem of nutrient delivery and waste-product accumulation within the scaffold is considered. Finally, in Section 8, we discuss the implications of the modelling results, and identify areas for future work.

2. Idealized setup and problem description

The general setup is as follows: The bone chamber of the bioreactor comprises a porous scaffold, with typical pore diameter δ, occupying a circular cylindrical chamber of radius a and height $2h$. The chamber is filled with a fluid culture medium, which is assumed to be Newtonian and incompressible, with uniform density ρ and dynamic viscosity μ. Flow is forced through the chamber via inlet and outlet pipes, and also through N identical porous-walled fibres of length 2ℓ inserted through the scaffold. Fluid is injected at one end of each fibre and the other end is sealed, so that the fluid is emitted through the porous walls into the scaffold. See Fig. 3 for one possible configuration.

We adopt a Cartesian coordinate system (x, y, z) to describe positions within the bioreactor chamber. The fluid velocity $\boldsymbol{u}$ and pressure p in the pore space and within the fibres are governed by the incompressible Navier–Stokes equations (see, e.g. Batchelor, 1967):

$$\nabla \cdot \boldsymbol{u} = 0, \quad \rho \frac{\partial \boldsymbol{u}}{\partial t} + \rho(\boldsymbol{u} \cdot \nabla)\boldsymbol{u} = -\nabla p + \mu \nabla^2 \boldsymbol{u}. \tag{1}$$

Boundary conditions are no-penetration and no-slip (i.e. $\boldsymbol{u} = \boldsymbol{0}$) on the chamber walls and on the scaffold pore and fibre surfaces, together with appropriate flux conditions at the various inlets and outlets.

The volume flux from the inlet pipe is Q_+, and the flux injected into each fibre Q_f. Since the fluid is assumed to be incompressible, the flux at the outlet is then $Q_- = Q_+ + NQ_f$. The fluxes Q_+ and Q_f are regarded as input parameters, since they are typically set by the experimentalists using volumetric pumps. The local flux per unit length emitted from each axial position along each fibre is denoted $q(s)$, where s measures distance along the fibre. We therefore have

$$Q_f = \int_{-\ell}^{\ell} q(s)\,\mathrm{d}s. \tag{2}$$

Whereas the total flux Q_f from each fibre is a known input parameter, the distribution $q(s)$ along their length must be determined as part of the solution to the combined flow problem in the fibres and the scaffold.

We now describe in detail three specific configurations of inlet/outlet pipes and fibres, which we shall use as examples to illustrate our modelling approach. The configurations are depicted in Fig. 4. We note that all have a certain degree of symmetry, since this is more likely to give a favourable (i.e. more uniform) flow field. Cylindrical chambers are used because of their ease of manufacture.

- Configuration A is shown in detail in Fig. 3. Inlet and outlet pipes are situated on opposite sides of the curved surface, and two porous fibres run across the scaffold in the perpendicular

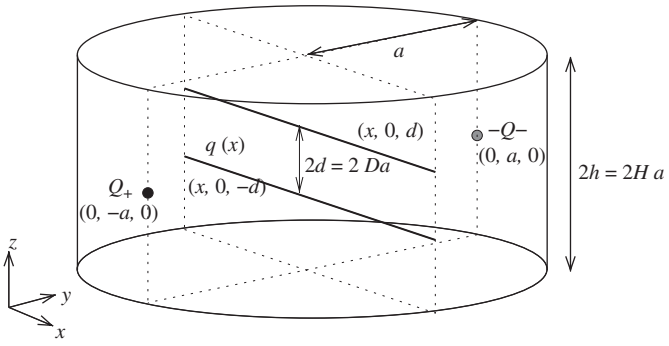

Fig. 3. An overview of the bioreactor chamber in configuration A, showing the positions of the inlet and outlet pipes (marked with filled circles), and the two porous fibres (solid lines). The other configurations are shown in less detail in Fig. 4.

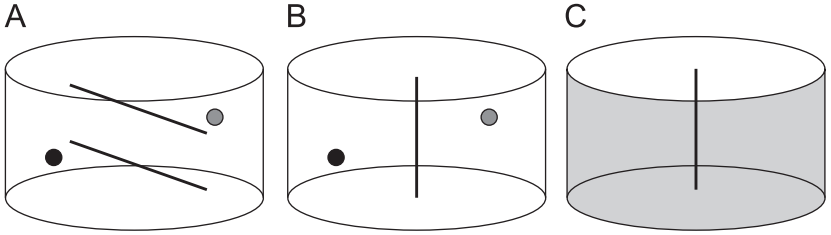

Fig. 4. Sketches of the bioreactor chamber, showing the three configurations of inlet/outlet pipes (filled circles) and porous fibres (thick lines) considered here. A more detailed view of configuration A is shown in Fig. 3. In configuration C, the whole of the cylindrical surface acts as a distributed outlet.

direction. The length of the fibres is $2\ell = 2a$, and they lie a distance d above and below the mid-plane of the chamber. This configuration is based on the bioreactor prototype currently under development (see Cartmell et al., 2007).
- Configuration B has the same inlet and outlet pipes as in A, but there is a single fibre running vertically along the axis of the cylinder ($2\ell = 2h$).
- Configuration C retains the vertical fibre of B. However, instead of the inlet and outlet pipes, the fluid only enters through the vertical fibre and the whole of the cylindrical surface acts as a distributed outlet.

The distributed outlet in configuration C is different from the outlet pipes used in A and B. It is realized by having a bioreactor chamber of a larger radius than that of the scaffold, so that fluid is able to exit the scaffold in all radial directions. The ease of free flow out of the scaffold relative to flow within the scaffold ($\delta \ll a$) means that the pressure variations outside the scaffold will be minimal compared with those inside. Therefore, in this case, we effectively have a constant pressure boundary condition on $x^2 + y^2 = a^2$.

In each configuration, we consider the flow in the scaffold and the flow in the fibres as two separate problems, coupled by the continuity of pressure and volume flux per unit area at the outside of the fibre walls. In both regions the full Navier–Stokes equations and complicated geometries can be simplified leading to tractable problems. We now consider the scaffold and fibre problems in turn.

Table 1
Dimensions and typical physical properties of the bioreactor setup being developed by Cartmell and Michael.

Quantity	Symbol	Typical value
Internal radius of chamber	a	7.5×10^{-3} m
Internal height of bone section	$2h$	1.0×10^{-2} m
Length of each porous fibre	2ℓ	10^{-2} m[a]
External radius of porous fibres	b_w	5×10^{-4} m
Internal radius of porous fibres	b_c	1.7×10^{-4} m
Internal radius of inlet/outlet pipes	d	5×10^{-4} m
Pore diameter of scaffold	δ	6.8×10^{-4} m
Porosity of scaffold	ϕ	0.8
Tortuosity of scaffold	τ	1.15
Permeability of scaffold	k	2×10^{-9} m^2
Typical pore diameter in fibre wall	δ_w	1×10^{-7} m
Mean radial permeability of fibre wall	k_w	1×10^{-17} m^2
Density of culture medium	ρ	1×10^3 kg m^{-3}
Viscosity of culture medium	μ	7×10^{-4} kg m^{-1} s^{-1}
Typical total volume flux	Q_-	1×10^{-7} m^3 s^{-1}

Lengths measured from experimental apparatus. Scaffold properties from analysis of MicroCT data; permeability and tortuosity estimates detailed in Appendix A.1. Fibre permeability estimate explained in Appendix A.2. Culture medium properties measured experimentally at 37 °C.

[a] The length of the fibres in the bioreactor depends on their position and orientation. In the configurations we consider here, we have either $\ell = a$ or h.

3. Flow within the scaffold

A MicroCT image of a typical scaffold is shown in Fig. 2A. The pore geometry is of a random nature, with about 30 pores over the height of the scaffold. All the pores appear to be interconnected. We model the scaffold as a porous medium (see, e.g. Bear, 1988), with a typical pore diameter δ, porosity ϕ (the volume fraction of pore space), and tortuosity τ (defined as the average ratio of streamline lengths to the straight-line distance between two points).[1] Typical values for these parameters are given in Table 1.

The ratio of inertial and viscous effects is given by the pore Reynolds number

$$Re_p = \frac{\rho \mathscr{U} \delta}{\mu}, \tag{3}$$

where $\mathscr{U}$ is a typical interstitial velocity. We estimate $\mathscr{U}$ by dividing the typical volume flux Q_- by the typical cross-sectional area of pore space $2\phi ah$. This is then modified by a factor of the scaffold tortuosity τ. (The more tortuous the scaffold, the faster the interstitial flow has to be to travel the longer paths in the same time.) Therefore

$$\mathscr{U} \sim \frac{\tau}{\phi} \frac{Q_-}{2ah}, \tag{4}$$

and using the data in Table 1, we obtain

$$Re_p \sim \frac{\rho \tau Q_- \delta}{2\phi ah\mu} \approx 2 \tag{5}$$

as an estimate for the pore Reynolds number.

The large number of pores and the not-too-large pore Reynolds number make it appropriate to use Darcy's law (see, e.g. Batchelor, 1967; Bear, 1988) to model the flow of culture medium through the scaffold. We model the scaffold as an isotropic porous medium, with a uniform permeability k. (See Appendix A.1 for a discussion of how to estimate k.)

Although the growth of the bone will alter this permeability, such growth occurs over a period of several days, which is much longer than the minutes required for fluid circulation. The slow variations of k can be captured using a 'quasi-static' approximation, i.e. assuming that at any instant the solution is as it would be with a constant value of k set by its instantaneous value. For simplicity, and because such variations are likely to be small, we shall just work with single fixed value of k in this paper.

Darcy's law is used to relate the Darcy velocity $\boldsymbol{v}$ to the interstitial pressure p.[2] Conservation of fluid is expressed in terms of a source strength per unit volume $\psi(\boldsymbol{x})$. We have

$$\boldsymbol{v} = -\frac{k}{\mu} \nabla p, \quad \nabla \cdot \boldsymbol{v} = \psi. \tag{6}$$

The various sources are modelled as points and lines and hence appear as delta functions in ψ. Away from these sources $\psi = 0$.

Since the diameter of the porous fibres and the inlet and outlet pipes are comparable with the pore size (see Table 1), it is consistent to model them as line and point sources, respectively. This simplifies the analysis, and reflects the fact that the actual size of the fibres and pipes, and detailed flow distribution near them, have little effect on the bulk flow in the scaffold.

Obviously, the point-source approximations will not be valid in the region surrounding the real source within a few pore diameters. Thus when interpreting the results, allowance must be made for the fact that the diverging velocities, pressures and shear stresses in the neighbourhood of the sources are in fact bounded and rise only to a magnitude of the order of that

[1] Note that there are several different definitions of tortuosity in use by various authors. In particular, the quantity referred to as tortuosity in Bear (1988) is τ^2 in the notation used here. The equations are unaffected by this different nomenclature.

[2] The Darcy velocity is a local average of the true interstitial velocity, taken over a volume that includes both the pore space and the solid scaffold. Hence, on the macroscale, $\boldsymbol{v}$ gives the volume flux of fluid per unit cross-sectional area. The interstitial pressure is the local average of the fluid pressure in the pore space.

predicted a few pore diameters away. Formally, the model represents an 'outer' solution away from the sources, and a separate 'inner' solution would be needed to accurately describe the flow in the neighbourhood of the sources. Such a solution would require knowledge of the detailed pore structure around the source, and is beyond the scope of this study.

3.1. Non-dimensionalization

We non-dimensionalize all lengths with the chamber radius a, so in non-dimensional coordinates $(X,Y,Z)=(x,y,z)/a$, the chamber occupies

$$X^2+Y^2\leqslant 1,\quad -H\leqslant Z\leqslant H, \tag{7}$$

where $H=h/a$ is the aspect ratio of the chamber. We non-dimensionalize the fluxes with respect to Q_-, so that the dimensionless total flux from the fibres is given by

$$\mathscr{Q}=\frac{NQ_f}{Q_-}. \tag{8}$$

The dimensionless flux from each fibre is then $\mathscr{Q}/N$, and the dimensionless flux from the inlet pipe is $1-\mathscr{Q}$. The distance s along the fibre is non-dimensionalized on the length a, and we introduce $\zeta=s/a$. The local flux per unit length $q(s)$ emitted from each point along the fibre is non-dimensionalized by writing

$$q(s)=\frac{Q_f}{a}\theta(\zeta)=\frac{Q_-}{a}\frac{\mathscr{Q}}{N}\theta(\zeta). \tag{9}$$

We non-dimensionalize velocities, pressure, and source strength in the natural way by writing

$$\boldsymbol{v}=\frac{Q_-}{a^2}\boldsymbol{V},\quad p=p_0+\frac{\mu Q_-}{ak}P,\quad \psi=\frac{Q_-}{a^3}\Psi. \tag{10}$$

The pressure must be considered relative to a reference pressure $p_0\equiv p(\boldsymbol{x_0})$ taken at a particular point $\boldsymbol{x_0}$ in the scaffold. This is because the scale Q_-/ak is only for *variations* in pressure within the scaffold, independent of any additive constants. For each configuration, we choose $\boldsymbol{x}_0$ to be a convenient point in the scaffold away from the singularities caused by the fibres and the inlet and outlet pipes. For configuration A, we set $\boldsymbol{x}_0=\boldsymbol{0}$, so the dimensionless pressure is zero at the centre of the scaffold. For configuration B, we set $\boldsymbol{x}_0=(a/2,0,0)$. Finally, for configuration C, we set $\boldsymbol{x}_0=(a,0,0)$ so that the dimensionless pressure is zero on the curved surface of the scaffold.

3.2. Dimensionless equations and boundary conditions

In terms of the non-dimensional variables, Darcy's equation and the continuity equation (6) become

$$\boldsymbol{V}=-\boldsymbol{\nabla}P,\quad \boldsymbol{\nabla}\cdot\boldsymbol{V}=\Psi. \tag{11}$$

Combining the two equations in (11), we obtain an equation for the dimensionless pressure:

$$\nabla^2P=-\Psi_{\text{inlet}}+\Psi_{\text{outlet}}-\Psi_{\text{fibres}}, \tag{12}$$

where the terms on the right-hand-side each correspond to one of the sources or sinks in the obvious way. This equation is then solved within the scaffold, subject to appropriate boundary conditions, to find P. The physical boundary conditions generally involve the fluid velocity $\boldsymbol{V}$, and so must be re-written in terms of P using (11), so they can be applied to (12). Once P is known, (11) is used to recover $\boldsymbol{V}$ and complete the solution in the scaffold. We now present the source functions and boundary conditions on P for each of the three configurations.

3.2.1. Configuration A

The fibre source is given by

$$\Psi_{\text{fibres}}=\tfrac{1}{2}\mathscr{Q}\theta(X)\delta(Y)(\delta(Z-D)+\delta(Z+D)), \tag{13}$$

representing two fibres running along $y=0$, $z=-d$ and $y=0$, $z=d$, from $x=-1$ to 1. The vertical separation of the fibres is $2D=2d/a$, and $\delta(\cdot)$ is the delta function. The rate of fluid emission by the fibres varies along their length and is given by $\frac{1}{2}\mathscr{Q}\theta(X)$, where $\theta(X)$ is as yet unknown. The inlet and outlet sources are given by

$$\Psi_{\text{inlet}}=2(1-\mathscr{Q})\delta(X)\delta(Y+1)\delta(Z), \tag{14}$$

$$\Psi_{\text{outlet}}=2\delta(X)\delta(Y-1)\delta(Z), \tag{15}$$

for an inlet at $(0,-1,0)$ and an outlet at $(0,1,0)$, respectively. Since the point sources are located on the domain boundary, the strengths are doubled in the above expression to obtain the correct fluxes inside the domain.

Using (11), the boundary conditions resulting from no normal flow through the walls of the chamber are

$$\hat{\boldsymbol{n}}\cdot\boldsymbol{\nabla}P=0\quad\text{on } X^2+Y^2=1,\quad \frac{\partial P}{\partial Z}=0\quad\text{on } Z=\pm H, \tag{16}$$

where $\hat{\boldsymbol{n}}$ is the unit normal to the curved walls. The definition of $\boldsymbol{x}_0$ means that the pressure origin is set by $P(0,0,0)=0$.

3.2.2. Configuration B

The fibre source is now

$$\Psi_{\text{fibres}}=\mathscr{Q}\theta(Z)\delta(Y)\delta(Z). \tag{17}$$

The inlet and outlet source terms and the boundary conditions are identical to (14)–(16) as used in configuration A. The pressure origin is set by $P(\frac{1}{2},0,0)=0$, from the choice of $\boldsymbol{x}_0$.

3.2.3. Configuration C

The fibre source is as in configuration B:

$$\Psi_{\text{fibres}}=\mathscr{Q}\theta(Z)\delta(Y)\delta(Z). \tag{18}$$

However, there are no point inlet or outlet sources, so

$$\Psi_{\text{inlet}}=\Psi_{\text{outlet}}=0. \tag{19}$$

Instead, the distributed outlet modifies the boundary condition on the curved surface, which becomes

$$P=0\quad\text{on } X^2+Y^2=1, \tag{20}$$

representing the fact that the pressure gradients required to drive flow in the region outside the scaffold are much smaller than those required inside. The no normal flow condition on the upper and lower chamber walls remains

$$\frac{\partial P}{\partial Z}=0\quad\text{on } Z=\pm H. \tag{21}$$

In all three configurations, the dimensionless flux per unit length $\theta(\zeta)$ from the fibres depends on the conditions applied at the fibre ends and the properties of the fibre. If $\theta(\zeta)$ is known, then (8), (12), and the appropriate equations from (13) to (21) form a well-posed problem for the pressure P within the scaffold. We now determine $\theta(\zeta)$ by analysing the flow in the fibres.

4. Flow in the fibres

The porous fibres are modelled as circular cylinders of length 2ℓ and external diameter $2b_w$, with a hollow core of internal diameter $2b_c$. See Fig. 5. We use cylindrical polar coordinates (r,φ,s) aligned with the fibre. In configuration A, we have $s=x$,

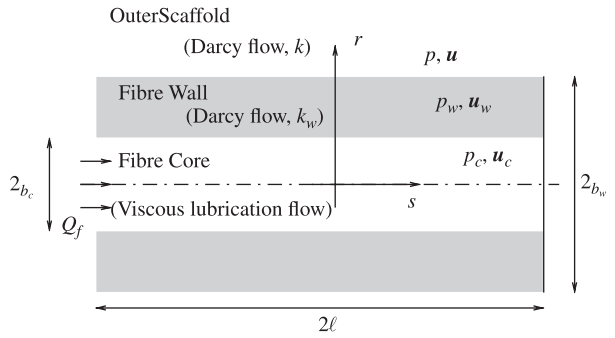

Fig. 5. The geometry of the porous-walled fibres, together with the coordinates and variables used to describe the flow within them.

$r^2 = y^2 + (z \pm d)^2$, and $\ell = a$ (see Fig. 3). In configurations B and C, we have $s = z$, $r^2 = x^2 + y^2$, and $\ell = h$.

The fibre walls are modelled as an axisymmetric and axially uniform porous medium, governed by Darcy's law. The radial component of the permeability tensor $\mathbf{k}_w$ is denoted $k_w(r)$, and the other principal components are assumed to be no larger than k_w. In practice, the fibre pores are aligned predominantly in the radial direction (see Fig. 2B), so that the resistance to radial flow is significantly less than the resistance in any other direction, and the radial permeability is greater than the other components.

Pressures are denoted by p and velocities by $\boldsymbol{u} = (u, v, w)$ with components in the cylindrical polar coordinates defined above. We use subscripts c for the core and w for the walls. In the porous walls, $\boldsymbol{u}_w$ represents the Darcy velocity. Boundary conditions are provided by continuity of pressure and radial volume flux per unit area at $r = b_w$, together with the imposed inlet flux Q_f at $s = -\ell$, and zero outlet flux at $s = \ell$. Assuming the axial flux is dominated by the flow in the core, the flux conditions at the ends of each of the fibres can be written as

$$2\pi \int_0^{b_c} w_c(r, -\ell) r \, \mathrm{d}r = Q_f, \quad 2\pi \int_0^{b_c} w_c(r, \ell) r \, \mathrm{d}r = 0. \tag{22}$$

A number of separations of scales help simplify the analysis of the flow in the fibre, which follows below in Sections 4.3–4.5. We assume that the fibre is slender ($b_c/\ell \ll 1$) and that the walls are relatively impermeable ($k_w \ll b_c^2$, $k_w \ll k$). Both these assumptions are justified by the experimental setup (see Table 1). We show that this regime leads to predominantly axial flow in the fibre core, and predominantly radial flow in the fibre walls. We also show that the pressure difference across the fibre wall is large compared with both the pressure drop along the length of the fibre, and the typical pressure variations within the surrounding scaffold. This means that we can solve for the flow in the fibre without needing to know the details of the flow and pressure fields in the scaffold. Since the flow in the scaffold has no effect on the flow in the fibre, there is no source of asymmetry, and we may assume axisymmetric flow in the fibre, i.e. $v \equiv 0$, and no dependence on the azimuthal angle φ.

4.1. Non-dimensionalization

We begin by introducing two non-dimensional parameters

$$\varepsilon = \frac{b_c}{a} \ll 1, \quad \lambda = \frac{b_w}{b_c} = O(1), \tag{23}$$

which describe the aspect ratio and relative wall thickness of the fibre.

The radial and axial coordinates are non-dimensionalized by the inner fibre radius b_c and chamber radius a, respectively,

$$\xi = \frac{r}{b_c} = \frac{r}{\varepsilon a}, \quad \zeta = \frac{s}{a}. \tag{24}$$

The core then occupies $0 < \xi < 1$ and the wall $1 < \xi < \lambda$. The non-dimensional length of the fibre is $2L = 2\ell/a = O(1)$, so $-L < \zeta < L$. In configuration A, we have $L = 1$, while in configurations B and C we have $L = H$.

We define a mean radial permeability $\bar{k}_w$ for the fibres as the permeability that would give a radially uniform fibre the same radial flux for a given transmural pressure difference. As shown in Appendix A.2, this implies

$$\frac{1}{\bar{k}_w} = \frac{1}{\ln \lambda} \int_{b_c}^{b_w} \frac{1}{r k_w(r)} \, \mathrm{d}r. \tag{25}$$

We now non-dimensionalize the permeability as

$$k_w(r) = \bar{k}_w K_w(\xi). \tag{26}$$

The non-dimensionalization of the axial velocity in the core and the radial velocity in both the core and the wall is based on the imposed flux Q_f:

$$w_c = \frac{Q_f}{b_c^2} W_c, \quad u_c = \frac{Q_f}{b_c a} U_c, \quad u_w = \frac{Q_f}{b_c a} U_w. \tag{27}$$

The axial velocity w_w in the wall is assumed to be much smaller than w_c, since the flow resistance is much larger in the wall.

The pressure p is scaled with the pressure difference required to drive the flux Q_f radially outwards through the fibre walls since, for relatively impermeable walls, this is expected to be the largest resistance to overcome, and hence will result in the largest pressure drop. We therefore write

$$p_c = p_0 + \frac{\mu Q_f \ln \lambda}{a \bar{k}_w} P_c, \quad p_w = p_0 + \frac{\mu Q_f \ln \lambda}{a \bar{k}_w} P_w. \tag{28}$$

4.2. Boundary conditions

At the ends of the fibres, we apply the flux conditions (22). In dimensionless form these are

$$2\pi \int_0^1 W_c(\xi, -L) \xi \, \mathrm{d}\xi = 1, \quad 2\pi \int_0^1 W_c(\xi, L) \xi \, \mathrm{d}\xi = 0. \tag{29}$$

At $\xi = 1$, the boundary between the fibre wall and the core, we impose continuity of the normal velocity and pressure, giving

$$U_c(1, \zeta) = U_w(1, \zeta), \quad P_c(1, \zeta) = P_w(1, \zeta). \tag{30}$$

Since the fibre wall is rigid and relatively impermeable, we have an effective no-slip condition on the axial flow in the core:

$$W_c(1, \zeta) = 0. \tag{31}$$

At $\xi = \lambda$, the outer edge of the fibre wall, we impose continuity of radial flux and pressure. The flux condition yields an expression for θ:

$$\theta(\zeta) = \oint_0^{2\pi} U_w(\lambda, \zeta) \lambda \, \mathrm{d}\varphi = 2\pi\lambda U_w(\lambda, \zeta). \tag{32}$$

Using (10) and (28), the pressure condition is

$$P_w(\lambda, \zeta) = \frac{N}{\mathscr{Q} \ln \lambda} \frac{\bar{k}_w}{k} P. \tag{33}$$

As both P and P_w are $O(1)$, and the remaining factor on the right-hand side is very small ($\bar{k}_w \ll k$; see Table 1), it is appropriate to approximate

$$P_w(\lambda, \zeta) = 0. \tag{34}$$

We now proceed to solve for the flow and pressure field inside the fibres. The general strategy is to express all the variables in terms of the pressure P_c in the core, and then apply the boundary conditions to obtain a single equation for P_c, which we solve. Once P_c is found, the other variables can be recovered.

4.3. Flow in the fibre core

The flow in the core is governed by the (dimensional) steady Navier–Stokes equations

$$\boldsymbol{\nabla}\cdot\boldsymbol{u}_c = 0, \tag{35}$$

$$\rho(\boldsymbol{u}_c\cdot\boldsymbol{\nabla})\boldsymbol{u}_c = -\boldsymbol{\nabla}p_c + \mu\nabla^2\boldsymbol{u}_c. \tag{36}$$

Since the tube is slender, we use a viscous lubrication approximation (see, e.g. Ockendon and Ockendon, 1995) to neglect inertia and radial pressure gradients. This relies on the reduced Reynolds number Re_c being small, a condition we verify in Appendix Appendix B. In the dimensionless variables defined in (24), (27) and (28) the equations reduce to

$$P_c = P_c(\zeta), \tag{37}$$

$$\frac{\mathrm{d}P_c}{\mathrm{d}\zeta} = \frac{\alpha^2}{16}\frac{1}{\xi}\frac{\partial}{\partial\xi}\left(\xi\frac{\partial W_c}{\partial\xi}\right), \tag{38}$$

$$\frac{\partial W_c}{\partial\zeta} + \frac{1}{\xi}\frac{\partial}{\partial\xi}(\xi U_c) = 0, \tag{39}$$

where we have introduced the dimensionless parameter

$$\alpha^2 = \frac{16\bar{k}_w}{\varepsilon^4 a^2\ln\lambda}, \tag{40}$$

which is a measure of the resistance to axial flow through the core compared with that of radial flow out through the walls. The boundary conditions are given by (29)–(31).

We now integrate (38) twice with respect to ξ. One constant is set by regularity at $\xi = 0$, and the other by the boundary condition (31) at $\xi = 1$. We obtain the Poiseuille flow

$$W_c = -\frac{4}{\alpha^2}\frac{\mathrm{d}P_c}{\mathrm{d}\zeta}(1-\xi^2). \tag{41}$$

Using mass continuity (39) we recover the radial velocity. The single constant of integration is set by regularity at $\xi = 0$. We obtain

$$U_c = \frac{1}{\alpha^2}\frac{\mathrm{d}^2P_c}{\mathrm{d}\zeta^2}\xi(2-\xi^2). \tag{42}$$

Substituting for W_c, the flux conditions (29) can be written in terms of P_c as

$$\left.\frac{\mathrm{d}P_c}{\mathrm{d}\zeta}\right|_{\zeta=-L} = -\frac{\alpha^2}{2\pi}, \quad \left.\frac{\mathrm{d}P_c}{\mathrm{d}\zeta}\right|_{\zeta=L} = 0. \tag{43}$$

4.4. Flow through the fibre wall

The flow within the porous wall is governed by Darcy's law, and conservation of mass:

$$\boldsymbol{u}_w = -\frac{1}{\mu}\mathbf{k}_w\cdot\boldsymbol{\nabla}p_w, \tag{44}$$

$$\boldsymbol{\nabla}\cdot\boldsymbol{u}_w = 0, \tag{45}$$

where $\boldsymbol{u}_w$ is the Darcy velocity. Boundary conditions arise from the continuity of fluxes and pressures at $r = b_c$ and b_w.

We now assume (subject to *a posteriori* verification in Appendix Appendix B) that the axial flow w_w is negligible in the continuity equation (45). (This is motivated by the need for a large radial pressure gradient to drive flow out through the walls, compared with a smaller axial pressure gradient linked to the axial flow in the core.) In non-dimensional form, the governing equations are then

$$U_w = -K_w(\xi)\ln\lambda\frac{\partial P_w}{\partial\xi}, \tag{46}$$

$$\frac{1}{\xi}\frac{\partial}{\partial\xi}(\xi U_w) = 0. \tag{47}$$

Boundary conditions are provided by (30), (32) and (34).

Substituting the expression (42) into the matching condition (30a) we obtain

$$U_w(1,\zeta) = \frac{1}{\alpha^2}\frac{\partial^2P_c}{\partial\zeta^2}. \tag{48}$$

Integrating (47) and applying (48), the radial velocity within the wall is

$$U_w(\xi,\zeta) = \frac{1}{\alpha^2}\frac{\partial^2P_c}{\partial\zeta^2}\frac{1}{\xi}. \tag{49}$$

We substitute this expression into (46), integrate with respect to ξ, and apply the boundary condition (34) at $\xi = \lambda$ to obtain

$$P_w(\xi,\zeta) = \frac{1}{\alpha^2}\frac{\partial^2P_c}{\partial\zeta^2}\frac{1}{\ln\lambda}\int_\xi^\lambda\frac{1}{\xi' K_w(\xi')}\,\mathrm{d}\xi'. \tag{50}$$

From the definitions (25) and (26), the integral is equal to $\ln\lambda$ at $\xi = 1$, hence

$$P_w(1,\zeta) = \frac{1}{\alpha^2}\frac{\partial^2P_c}{\partial\zeta^2}. \tag{51}$$

4.5. The flux emitted by the fibres

Applying the final boundary condition (30b) to equation (51), we obtain an equation for the variation of P_c along the length of the fibre:

$$\frac{\mathrm{d}^2P_c}{\mathrm{d}\zeta^2} - \alpha^2P_c = 0. \tag{52}$$

This equation is solved subject to (43), giving

$$P_c(\zeta) = \frac{\alpha}{2\pi}\frac{\cosh[\alpha(L-\zeta)]}{\sinh(2\alpha L)}. \tag{53}$$

With this solution, the flux $\theta(\zeta)$ emitted from the fibre into the outer scaffold can be derived from (32) and (49), and is

$$\theta(\zeta) = \frac{\alpha\cosh[\alpha(L-\zeta)]}{\sinh(2\alpha L)}. \tag{54}$$

The parameter α, defined in (40), encapsulates how easy it is push fluid out through the fibre walls compared with pushing it axially along the core. For $\alpha \gg 1$, it is relatively easy for fluid to exit the fibre through the walls. We then have

$$\theta(\zeta) \sim \alpha\mathrm{e}^{-\alpha(L+\zeta)}, \tag{55}$$

so almost all of the flux Q_f leaves through the wall within a distance of $O(\alpha^{-1})$ from the inlet at $\zeta = -L$. Since this is unlikely to offer any improvement over a bioreactor system without fibres, we reject this possibility, and assume $\alpha \leqslant O(1)$.

For $\alpha = O(1)$, we see a significant variation of θ along the fibre, which is also likely to offer less advantage than a uniform flux.

At the other extreme, $\alpha \ll 1$, we have

$$\theta(\zeta) \sim \frac{1}{2L} \tag{56}$$

so the emitted flux is uniform along the length of the fibre.

4.6. Summary

We have found the solution for the flow in the fibres. The pressure P_c in the core is given by (53) and this can be substituted back into the previous expressions for the other physical variables. The dimensionless flux per unit length θ emitted at each point along the length of the fibre is given by (54). This expression can now be used to complete the model for the flow in the scaffold developed in Section 3. In Appendix B, we confirm that the various approximations we have used are valid for the experimental setup being modelled.

Table 2
Typical values of the various dimensionless parameters appearing in Sections 2–4, computed from the values in Table 1.

H	ε	λ	k/a^2	$\bar{k}_w/b_c^2$	α^2
0.7	0.02	3	10^{-4}	10^{-6}	0.07

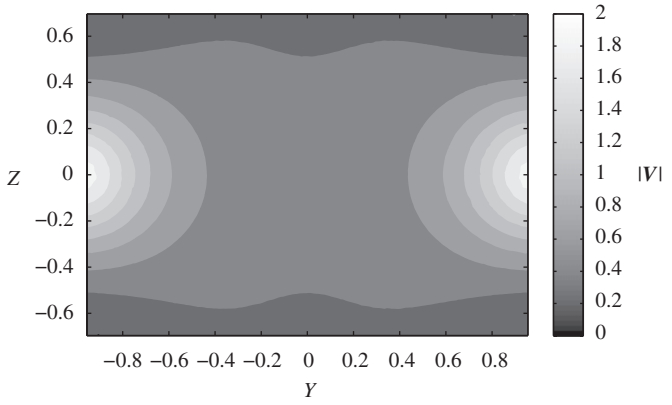

Fig. 6. The magnitude of the dimensionless Darcy velocity $\boldsymbol{V}$ in the vertical plane $X = 0.3$ in configuration A with $\mathcal{Q} = 0$ (i.e. no flux from the fibres). The inlet is out of the plane to the left, and the outlet lies similarly to the right. The two fibres run perpendicular to the plane through $Y = 0$, $Z = \pm 0.35$. From the dimensionless Darcy velocity, the dimensional equivalent can be recovered from (10), and an estimate for the shear stress found using (58).

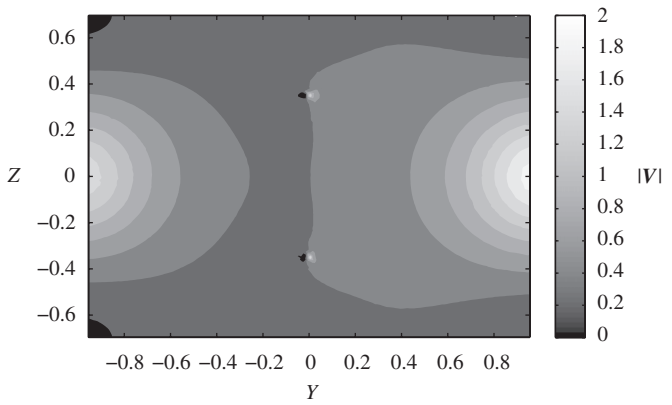

Fig. 7. The magnitude of the dimensionless Darcy velocity in the plane $X = 0.3$ in configuration A with $\mathcal{Q} = 0.2$. Other details as in Fig. 6. Flow is generally from left to right, and fluid is emitted by the fibres.

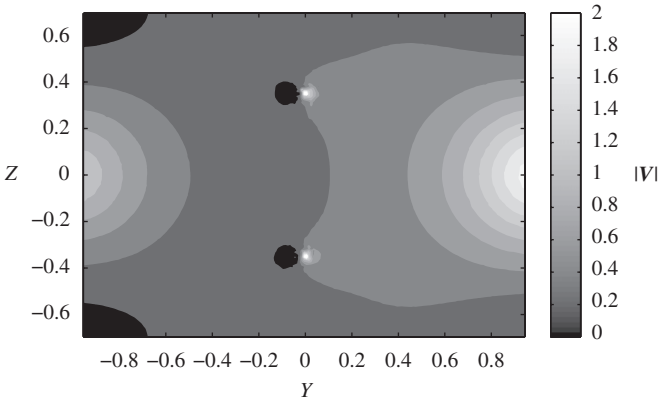

Fig. 8. The magnitude of the dimensionless Darcy velocity in the plane $X = 0.3$ in configuration A with $\mathcal{Q} = 0.4$. Other details as in Fig. 6. Flow is generally from left to right, and fluid is emitted by the fibres.

5. Numerical solutions for the fluid flow

In all the numerical computations, we take $\alpha \ll 1$ so that (56) holds and the flux emitted by the fibres is uniform along their length. A uniform flux is desirable from a theoretical standpoint, as it is likely to result in a more even distribution of culture medium flow and shear stresses. Furthermore, for the fibres being considered for use in the prototype bioreactors that motivated this study, we have $\alpha = O(10^{-1}) \ll 1$ (see (40) and Table 2).

With $\theta(\zeta)$ given by (56), the model developed in Section 3 then leads to the problem of solving Poisson's equation (12) for the pressure P in the cylindrical bioreactor chamber. We have Dirichlet and/or Neumann boundary conditions on the walls, and a number of delta-function source terms representing the fibres and inlet/outlet pipes. The equations and boundary conditions for the three fibre configurations considered in this paper are given in Section 3.2.

Similar systems of equations arise in many physical problems, and solution techniques are well-developed. We solved the system numerically using the Electrostatics package of the 'COMSOL Multiphysics' computer program,[3] which uses a finite element technique. Once the pressure P has been computed, the Darcy velocity $\boldsymbol{V}$ is determined from (11).

For each of the three configurations, the flow may be solved with typical parameter values to provide insight into how the fibres affect the flow. In all cases, we used an aspect ratio of $H = 0.7$, in line with the experimental prototype shown in Fig. 1. The graphs show the magnitude $|\boldsymbol{V}|$ of the Darcy velocity on a planar cross-section through the bioreactor chamber.

For configuration A, we used a fibre separation $2D = 0.7$ (see Fig. 3). Results are shown on an off-centre vertical plane perpendicular to the fibres at $X = 0.3$. We consider a fixed total flux Q_- with three different values of the proportion $\mathcal{Q}$ from the fibres: 0, 0.2, and 0.4. The results are shown in Figs. 6–8. Other parallel planes show essentially the same qualitative structure, with a dipole structure around the fibres and larger velocities in the vicinity of the inlet and outlet pipes. The off-centre planes were chosen to avoid the singularities at these points.

For configurations B and C, there is a single vertical fibre, and we use off-centre horizontal cross-sections at $Z = 0.3$ instead. For configuration B, we again present results for $\mathcal{Q} = 0, 0.2, 0.4$. See Figs. 9–11. For configuration C, there are no separate input flows so

[3] Developed and distributed by COMSOL Inc. Full details available online at http://www.comsol.com/.

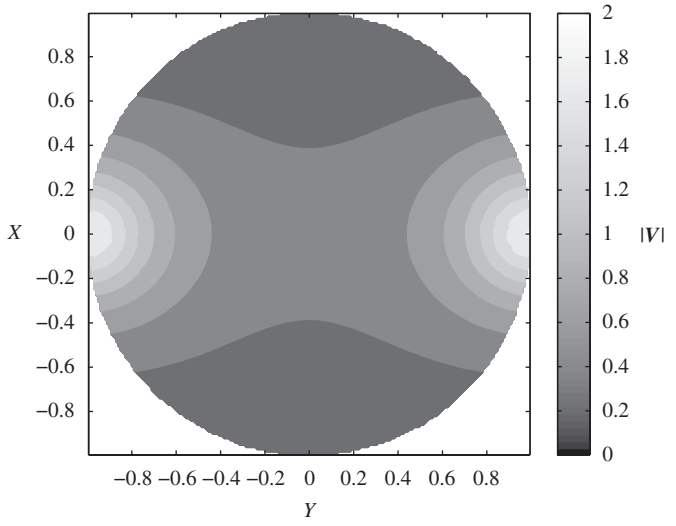

Fig. 9. The magnitude of the dimensionless Darcy velocity $\boldsymbol{V}$ in the plane $Z = 0.3$ in configuration B with $\mathscr{Q} = 0$ (no flow from the fibre). The single fibre runs perpendicular to the plane, through $X = Y = 0$. The inlet pipe is to the left and the outlet pipe to the right, both in the plane $Z = 0$. From the dimensionless Darcy velocity, the dimensional equivalent can be recovered from (10), and an estimate for the shear stress found using (58).

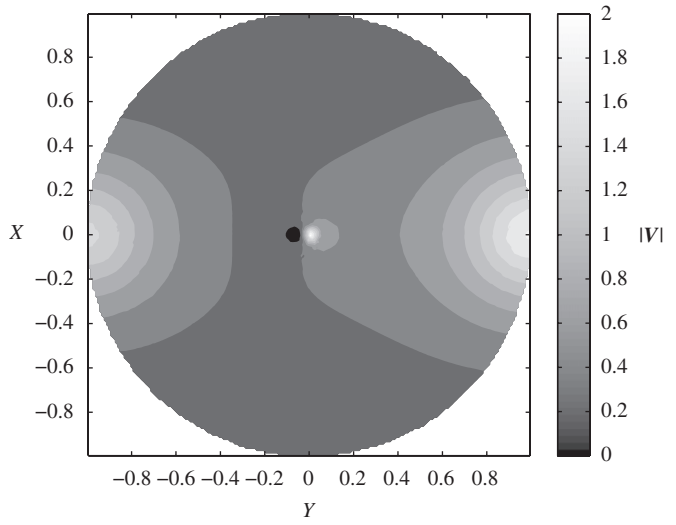

Fig. 10. The magnitude of the Darcy velocity in the plane $Z = 0.3$ in configuration B with $\mathscr{Q} = 0.2$. Other details as in Fig. 9. Flow is generally from left to right, with fluid emitted by the fibre.

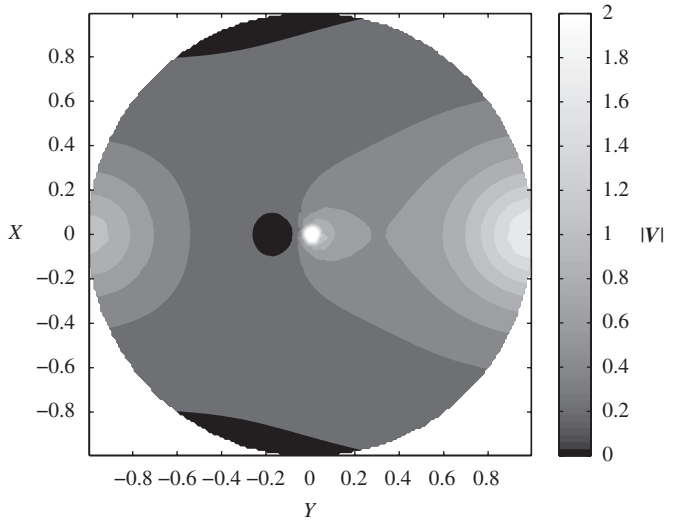

Fig. 11. The magnitude of the Darcy velocity in the plane $Z = 0.3$ in configuration B with $\mathscr{Q} = 0.4$. Other details as in Fig. 9. Flow is generally from left to right, with fluid emitted by the fibre.

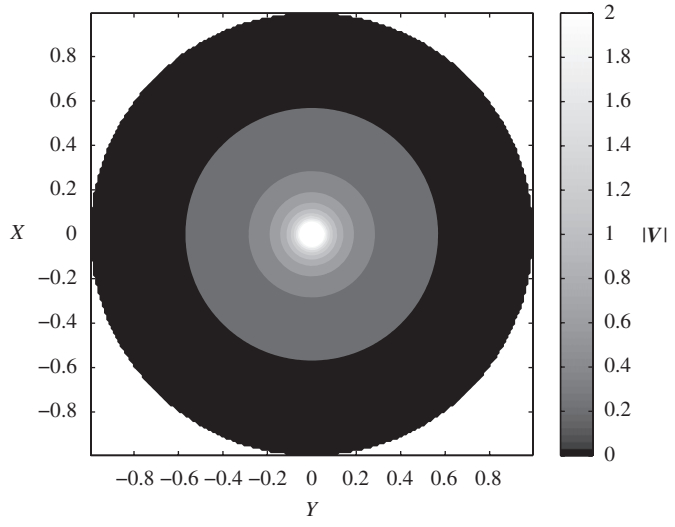

Fig. 12. The magnitude of the Darcy velocity in any horizontal plane $Z = Z_0$ in configuration C. Other details as in Fig. 9. Flow is radially outwards from the central fibre source.

$\mathscr{Q} \equiv 1$. The solution, which can be obtained analytically, is of purely radial flow, and is shown in Fig. 12.

The computations show that without the fibres ($\mathscr{Q} = 0$), flow rates are highest in the vicinity of the inlet and outlet pipes, as would be expected. The slowest regions of the flow are found near the chamber walls on the plane $Y = 0$. The addition of the fibres increases relative flow rates on the downstream side of them ($Y > 0$), but also decreases the flow on the upstream side ($Y < 0$). These increases and decreases become more pronounced as $\mathscr{Q}$ increases.

6. Shear stress

As discussed in the Introduction, bone cells are sensitive to fluid shear stresses. Some shear stress is necessary for viable growth, but higher levels may damage the cells. It is therefore important to calculate the shear-stress distribution associated with the flow fields computed in Section 5. The shear stresses will be proportional to the overall flow rate Q_-, which therefore needs to be adjusted so as to provide sufficient shear (and nutrient delivery) over as much of the scaffold as possible, while constraining excessively high shear to as small a region as possible.

The shear stress experienced by the cells within the individual scaffold pores can be estimated from the Darcy velocity as follows. We first take the estimate $\mathscr{U} \sim |\boldsymbol{v}|\tau/\phi$ for the mean magnitude of the interstitial velocity. We then use Poiseuille flow of mean velocity $\mathscr{U}$ through a circular duct of diameter δ as an approximate model for the local flow within each scaffold pore. With r as a local radial coordinate, the velocity profile is

$$v \approx 2\mathscr{U}\left[1 - \left(\frac{2r}{\delta}\right)^2\right] \tag{57}$$

Table 3
Typical values of the experimental parameters related to the nutrient problem.

Parameter	Symbol	Typical value
Time scale for fluid circulation	t_c	3.4×10^0 s
Time scale for cell growth	$t_{1/2}$	2×10^5 s
Time scale for culturing	t_g	6×10^5–3×10^6 s
Initial number of cells per unit volume	n_0	1×10^{12} cells m^{-3}

All values based on the experimental setup of Cartmell and Michael, apart from t_c which is calculated using (65). For other properties, see Table 1.

Table 4
Typical properties relating to two nutrients and a waste product that are relevant to the cells.

Nutrient or product	c_i^* (mol m^{-3})	$c_i^\dagger$ (mol m^{-3})	κ_i (m^2 s^{-1})	σ_i (mol cell^{-1} s^{-1})	t_{di} (s)
Glucose	5.6	0	7×10^{-10}	-8×10^{-17}	4.3×10^2
Oxygen (O_2)	1.0	0	3×10^{-9}	-4.2×10^{-17}	1.5×10^2
Lactic acid	0	0.4	1×10^{-9}	1.4×10^{-16}	1.8×10^1

The initial concentration c_i^* in the culture medium as it enters the bioreactor, the concentration $c_i^\dagger$ that would be detrimental to the cells, the diffusivity κ_i and the rate of production σ_i (negative in the case of uptake). Glucose concentration from culture medium product data (Invitrogen, 2008), and initial oxygen concentration based on solubility in water at 37 °C and 1 atm (Tromans, 1998). Approximate diffusivities for dilute solutions at 25–30 °C from Lide (2007), with the exception of lactic acid from Ribeiro et al. (2005). Typical uptake and production rates inferred from Komarova et al. (2000). The estimate for $c_i^\dagger$ for lactic acid is discussed in Appendix A.3. Depletion/accumulation times t_{di} calculated using (66), assuming $n = n_{\max} = 1.3 \times 10^{14}$ and $\phi = 0.8$.

and the wall shear stress is

$$S = \mu \left| \frac{\partial v}{\partial r} \right|_{(r=\delta/2)} \approx \frac{8\mu \mathscr{U}}{\delta} \approx \frac{8\mu\tau}{\phi\delta} |\boldsymbol{v}| = \frac{8\mu Q_- \tau}{\phi\delta a^2} |\boldsymbol{V}|. \tag{58}$$

The first two approximations for S use the velocity profile (57) and the estimate for $\mathscr{U}$ above; the final equality comes from the non-dimensionalization (10). While obviously not precise, (58) gives a reasonable estimate (at least in order-of-magnitude terms) for the shear stress experienced by the cells in terms of the local Darcy velocity and the fluid and scaffold properties. For the values given in Table 1 we obtain

$$S = \left(\frac{Q_-}{4.8 \times 10^{-6}\,\mathrm{m^3\,s^{-1}}} \right) |\boldsymbol{V}|\,\mathrm{Pa}. \tag{59}$$

From the numerical results, $|\boldsymbol{V}| = O(1)$ over most of the chamber, and exceeds 2 only in small regions near the fibres and inlet/outlet pipes. Thus, to obtain shear stresses of the order of Pascals (as in the experiments referenced in the Introduction), volume fluxes of the order of 10^{-5}–10^{-6} m^3 s^{-1} need to be used. This is somewhat higher than the anticipated value $Q_- \sim 10^{-7}$ m^3 s^{-1} in Table 1.

However, in any particular experiment, the desirable volume flux will depend on the requirements of the cells and on the exact properties of the bioreactor system being used. It may also be constrained by the availability of pumping equipment and the pressures required to force fluid through the system. We therefore leave the results in general terms, rather than trying to make definite predictions that may not apply in other situations. Another factor to consider is the effect of the flow rate upon nutrient and waste transport. This issue is addressed in the following section.

7. Nutrient and waste transport

One of the most important requirements for both survival and proliferation of the cells is the supply of nutrients and the removal of waste products. In the case of nutrients the supply must be sufficient to meet the demands of the proliferating cells, while in the case of waste products we need to ensure they are removed sufficiently rapidly to prevent any build-up that would be harmful. For example a build-up of lactic acid could cause a harmful change in pH (see A.3).

We use simple scaling arguments here to determine whether or not nutrient depletion or waste-product accumulation are significant effects over the relevant time scales in the culturing process. Key conclusions can be drawn without the need to solve the full system of equations explicitly.

Suppose that the cells are initially seeded on to the scaffold with a density n_0 per unit volume[4] and then proliferate over the culturing period. We assume a constant doubling time of $t_{1/2}$, so that the number of cells per unit volume at time t after the start of culturing is

$$n = n_0 \exp\left(\frac{t \ln 2}{t_{1/2}} \right). \tag{60}$$

The maximum cell density $n_{\max}$ is achieved when $t = t_g$ at the end of the culturing period. Typical values of n_0, $t_{1/2}$ and t_g, given in Table 3, indicate that the cells may double in number around 7 times over the culturing period t_g, leading to $n_{\max} \approx 1.3 \times 10^{14}$ m^{-3}.

The concentration c_i of an individual nutrient or waste product i in the fluid occupying the pore space of the scaffold is governed by an advection–diffusion equation

$$\frac{\partial c_i}{\partial t} + \boldsymbol{u} \cdot \boldsymbol{\nabla} c_i = \kappa_i \nabla^2 c_i, \tag{61}$$

where κ_i is the diffusivity of species i (assumed to be constant over the range of concentrations considered) and $\boldsymbol{u}(\boldsymbol{x})$ is the velocity of the fluid. Boundary conditions arise from the concentration in the culture medium at the inlets, and a flux condition describing uptake or production at the cell surfaces.

A simple averaged model describes each concentration field as a local average $\bar{c}_i$ (taken over the pore spaces), and includes the uptake or production by the cells as a source term. Following

[4] Note that this is number of cells per unit total volume of bioreactor chamber, not the number per unit volume of pore space.

e.g. Cogan and Keener (2004), we write

$$\phi\frac{\partial \bar{c}_i}{\partial t}+\boldsymbol{v}\cdot\boldsymbol{\nabla}\bar{c}_i=n\sigma_i+D_i\nabla^2\bar{c}_i, \tag{62}$$

where $\boldsymbol{v}$ is the Darcy velocity, $D_i=\phi\tilde{\kappa}_i/\tau^2$ is the effective diffusivity, and σ_i is the rate of production (negative in the case of uptake) of the species. The local diffusivity $\tilde{\kappa}_i$ is a modified version of the molecular diffusivity κ_i taking into account the effects of Taylor dispersion. We denote the concentration of species i at the inlet by c_i^*, and the concentration at which it becomes harmful to the cells as $c_i^\dagger$. Values of these parameters for three key species can be found in Tables 3 and 4.

The validity of constructing such an average depends on how much the local concentrations c_i deviate from the local mean $\bar{c}_i$ on the scale of the pores. This in turn is controlled by the ratio of advective to diffusive effects on that scale, a quantity known as the pore Péclet number

$$Pe_{\mathrm{p}i}=\frac{\delta^2\mathscr{U}}{a\kappa_i}. \tag{63}$$

Since $Pe_{\mathrm{p}i}=O(1)$ for the situation we are considering here, the use of the averaged-concentration model (62) is acceptable. In addition, the effects of Taylor dispersion will be small,[5] so we have $\tilde{\kappa}_i\approx\kappa_i$.

To non-dimensionalize (62), we first introduce a dimensionless concentration C_i, defined so that

$$C_i=\frac{\bar{c}_i-c_i^*}{c_i^\dagger-c_i^*}. \tag{64}$$

Then $C_i=0$ at the inlet, and $C_i=1$ corresponds to the concentration level that is detrimental to the cells (either a lack of a nutrient, or a harmful level of waste product). There are a number of key time scales in the problem, including the fluid circulation time (pore space volume scale divided by total flux)

$$t_{\mathrm{c}}=\phi a^3/Q_-, \tag{65}$$

the accumulation or depletion time (concentration change divided by production rate)

$$t_{\mathrm{d}i}=\frac{\phi(c_i^\dagger-c_i^*)}{\sigma_i n}, \tag{66}$$

and the growth time t_g for the cells. (See Tables 3 and 4.)

We non-dimensionalize lengths and velocities as in Section 3, and times based on the circulation time t_{c}, and write

$$\boldsymbol{v}=\frac{Q_-}{a^2}\boldsymbol{V},\quad t=t_{\mathrm{c}}T. \tag{67}$$

Substituting into (62), we obtain the governing equation for C_i:

$$\frac{\partial C_i}{\partial T}+(\boldsymbol{V}\cdot\boldsymbol{\nabla})C_i=\frac{1}{\gamma_i}+\frac{1}{Pe_i}\nabla^2C_i, \tag{68}$$

where

$$Pe_i=\frac{Q_-}{aD_i} \tag{69}$$

is the bulk Péclet number, and

$$\gamma_i=\frac{t_{\mathrm{d}i}}{t_{\mathrm{c}}}=\frac{(c_i^\dagger-c_i^*)Q_-}{\sigma_i n a^3} \tag{70}$$

is an inverse Damköhler number. This representation shows that the transport problems for the nutrients and waste products are mathematically equivalent.

[5] The correction in $\tilde{\kappa}$ due to Taylor dispersion scales as the square of the pore Péclet number with a numerically small pre-factor. Since $Pe_{\mathrm{p}i}=O(1)$, it is appropriate to neglect this correction.

The bulk Péclet number Pe_i gives the ratio of advective to diffusive effects over the scale of the whole bioreactor. With values in Tables 3 and 4, we have that $Pe_i\sim10^3\gg1$, so the concentration field is governed primarily by advection, with diffusion having little effect.

The inverse Damköhler number γ_i gives the ratio of the time t_{d} that it would take the cells to use up all the nutrient present at the initial concentration or to produce enough waste to reach harmful levels, to the time t_{c} that it takes the culture medium to circulate once through the bioreactor. For the case of nutrients this is also equal to the ratio of the input to cell usage rate. For waste products it is the ratio of the maximum removal rate (limited by the mass flux and the critical concentration level) to the rate of production by the cells. In terms of the non-dimensional time scale T, γ_i is the time scale for the nutrient or waste product to reach harmful levels in the absence of bulk transport in or out of the reactor. We also introduce $\Gamma=t_{\mathrm{g}}/t_{\mathrm{c}}$; the ratio of the culturing time of the cells to the circulation time of the culture medium.

For the species listed in Table 4, and $n=n_{\max}$, we find that $\gamma_i=126,44,5.3$ for glucose, oxygen and lactic acid, respectively. Therefore, towards the end of the culturing period harmful levels (particularly of lactic acid) can be reached within a few circulation times. So if the same parcel of culture medium undergoes more than a few cycles through the reactor chamber, harmful levels will be reached. It is therefore important that the culture medium is not continuously cycled in this manner; there must be some combination of a large external reservoir to dilute the changes in concentration that occur within the reactor and periodic replacement of the whole medium.

Since $\gamma_i\ll\Gamma\sim10^6$, harmful levels can also be reached over the course of the culturing in any stagnant or low-velocity regions where the culture medium remains for many circulation times. The physical bioreactor design should be optimized to reduce such regions and/or the overall flow rate increased to wash them out more quickly.

Of course, we have only considered three particular species in these calculations. Some of the nutrients in the culture medium are present in much lower concentrations than glucose. The role of some of the proteins present in the culture medium is not well understood and so it is difficult to model their depletion.

Nevertheless, the framework provided in this section allows the key parameters $Pe_{\mathrm{b}i}$, Pe_i, and γ_i to be calculated given additional data for any new species of interest. From these the relative importance of advection and diffusion can be estimated, as can the importance of depletion/accumulation over the course of the culturing.

8. Discussion and conclusions

In this paper, we have shown how simple mathematical modelling can be used as an alternative to experimental 'trial and error' or full CFD computations to investigate the flow and transport properties of a bioreactor system. While some of the specific results may indeed be useful in themselves, this paper is intended more to illustrate the general principle of the modelling, and to investigate the efficacy of including porous fibres as a new design feature. We have also identified several important dimensionless parameters that should be considered when designing bioreactor systems of this type.

While the modelling of the flow in the scaffold by Darcy's law lacks the precision and detail of full numerical calculations that take into account the detailed pore geometry (e.g. Porter et al., 2005; Boschetti et al., 2006), it provides good estimates of the

global flow field, shear stresses, and nutrient transport within the scaffold. The advantages of this approach are the Darcy model's simplicity, the ease and rapidity of obtaining results for many different scenarios, and the fact that by averaging the scaffold geometry, we do not require the detailed pore geometry, information that is expensive to obtain and, moreover, changes from one scaffold to another.

In terms of the shear stresses and nutrient transport within the bioreactor, we have shown how these may be estimated from the properties of the system under consideration. In particular, the theoretical approach can be used to guide the design of future systems. Using our framework, experimentalists can estimate in advance the range of flow rates required to achieve a desired shear-stress distribution and ensure sufficient nutrient and waste-product transport. They can also determine how often the culture medium may need to be replenished during the culturing.

Returning to the particular cases studied here, the results shown in Figs. 9–11 for configurations A and B suggest that adding fibres perpendicular to the main flow from the inlet and outlet pipes will probably not result in a beneficial change to the flow distribution. While there is an increase in the flow rates on the downstream side of the fibres, there is a corresponding decrease on the upstream side. However, perhaps oscillating the inlet/outlet or fibre flows may be able to counteract this. Nevertheless, the presence of the fibres can do little to increase flow rates in the stagnant corner regions, which are arguably the areas in need of most help.

The final configuration C fares much better. Using the fibre as the only source of fluid, and having a distributed outlet, ensures a more uniformly distributed flow. However, since the radial flux (radial velocity times $2\pi r$) is constant, higher velocities, and hence shear rates, are experienced near the axis. Depending on the precise sensitivity of the cells to the applied shear stress, this may or may not be problematic.

With regard to the fibres themselves, we have identified a key dimensionless parameter α, defined in (40), which is a function of the material properties and dimensions of the fibre. As discussed in Section 4.5, the value of α describes the relative ease of flow through the fibre walls compared with flow through the hollow fibre core. An outflow through the walls that is uniform along the length of the fibre is obtained if and only if $\alpha \ll 1$. Since we are interested in obtaining a uniform distribution of flow, this is the only regime we have considered in detail here. Knowledge of the pressures required to force a particular flow-rate through a particular fibre should prove useful in guiding the choice of fibre properties and pump setup.

Acknowledgements

This paper came about as an extension to a problem (Bailey et al., 2006) considered at the 6th Mathematics in Medicine Study Group, held at the University of Nottingham in September 2006, with funding from the Engineering and Physical Sciences Research Council (EPSRC).

The authors would also like to specifically acknowledge Jon Gittings and Irene Turner who manufacture the scaffolds (see Gittings et al., 2005) for the project that motivated this study.

Dr. Cartmell and Dr. Kuiper wish to acknowledge the financial support of a private local charity. Dr Waters is grateful to the EPSRC for funding in the form of an Advanced Research Fellowship. Dr. Cummings wishes to thank the City College of New York's Department of Chemical Engineering and Levich Institute for hospitality during a stay as a visiting professor.

Appendix A. Miscellaneous calculations and estimates

A.1. Permeability and tortuosity of the scaffold

The permeabilities and tortuosities of the scaffolds to be used in the system that motivated this study have not been determined experimentally, so we must rely on other data and results to estimate these parameters.

First we observe that the permeability k can be written as

$$k = \mathscr{C}\delta^2, \tag{A.1}$$

where δ is the typical pore diameter, and $\mathscr{C}$ is a dimensionless parameter that is a scale-independent function of the scaffold geometry. A theoretical calculation assuming the porous medium comprises randomly orientated equal circular pipes of diameter δ (see Bear, 1988, Section 5.10) gives

$$\mathscr{C} = \frac{\phi}{96}, \tag{A.2}$$

where ϕ is the porosity of the medium.

For similarly structured highly porous media, it is reasonable to believe $\mathscr{C} \propto \phi$. Haddock et al. (1999) have determined various properties of similar (though slightly less porous) hydroxyapatite scaffolds. Using their results (taking δ to be their quoted trabecular separation) we obtain

$$\mathscr{C} \approx \frac{\phi}{160}. \tag{A.3}$$

Pleasingly, this is the same order of magnitude as the theoretical estimate. We shall therefore use this value of $\mathscr{C}$ to estimate our permeability k. Using the values of ϕ and δ from Table 1, we obtain

$$k = \frac{\phi\delta^2}{160} = 2.3 \times 10^{-9}\,\mathrm{m}^2. \tag{A.4}$$

For the tortuosity, various empirical and theoretical estimates all give similar curves for tortuosity τ as a function of porosity ϕ (see, for example Koponen et al., 1996; Yu and Li, 2004). For $\phi = 0.8$, these formulae typically predict tortuosity values in the range 1.1–1.2. Since our results are not particularly sensitive to the actual value, we shall simply assume a value of $\tau = 1.15$.

A.2. Permeability of the fibre walls

An estimate for the mean radial permeability of the fibre walls can be determined from experimental data as follows. Assuming axisymmetric flow under a purely radial pressure gradient, Darcy's equation becomes

$$u_w(r) = \frac{k_w(r)}{\mu}\frac{\partial p}{\partial r}. \tag{A.5}$$

Conservation of mass implies that the radial flux q (per unit length of fibre) at each value of r is conserved, so

$$u_w(r) = \frac{q}{2\pi r}. \tag{A.6}$$

Eliminating u_w between (A.5) and (A.6), we obtain

$$\frac{\partial p}{\partial r} = \frac{\mu q}{2\pi r k_w(r)}. \tag{A.7}$$

Therefore the pressure difference ΔP between the core at $r = b_c$ and the outer surface at $r = b_w$ is given by

$$\Delta P = \frac{\mu q}{2\pi}\int_{b_c}^{b_w} \frac{1}{r k_w(r)}\,\mathrm{d}r. \tag{A.8}$$

Therefore a fibre with a uniform permeability $\bar{k}_w$ has the same overall resistance to radial flow as one with variable permeability

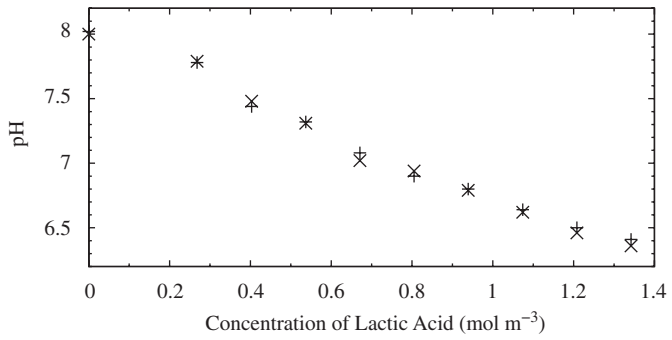

Fig. A1. The results of two titrations lactic acid into a typical culture medium to assess the level of buffering present. The culture medium comprised D-MEM (Invitrogen, 2008) with 10% fetal calf serum. Lactic acid was added drop-wise using a pipette, and data points comprising the volume added together with the pH of the solution were recorded. The agreement between the two titrations indicates good reproducibility.

$k_w(r)$ if and only if

$$\int_{b_c}^{b_w} \frac{1}{r\bar{k}_w}\,\mathrm{d}r = \int_{b_c}^{b_w} \frac{1}{rk_w(r)}\,\mathrm{d}r, \tag{A.9}$$

which is the definition for $\bar{k}_w$ used in (25). Using this definition to eliminate $k_w(r)$ from (A.8), we find that

$$\bar{k}_w = \frac{\mu q}{2\pi\Delta P}\ln\left(\frac{b_w}{b_c}\right). \tag{A.10}$$

Preliminary experimental data from Ellis and Chaudhuri (unpublished) suggests an order of magnitude estimate of $\bar{k}_w \sim 10^{-17}\,\mathrm{m}^2$, but this figure is likely to be quite sensitive to changes in the manufacturing conditions.

A.3. Harmful concentration of lactic acid

In this appendix, we describe how we estimate the concentration of lactic acid that would be harmful to the growing cells (see Table 4). When the pH drops the proliferation of cells is strongly inhibited. Each molecule of glucose produces two molecules of lactic acid and so the rate of production of lactic acid is twice the rate of glucose consumption.

The culture medium is initially at a pH of 8, and we assume that the growing cells can tolerate a pH change of up to ± 0.5, though growth rates are likely to be affected near to the extremities of this range.

In this pH range, lactic acid is almost fully dissociated and so behaves as a strong acid. Therefore in the absence of buffering the concentration of lactic acid required to cause a drop from 8 to 7.5 is given by

$$(10^{-7.5} - 10^{-8})\,\mathrm{mol\,dm^{-3}} \approx 2\times 10^{-5}\,\mathrm{mol\,m^{-3}}. \tag{A.11}$$

This is a tiny amount relative to the rates at which lactic acid is known to be produced by the cells, so it is therefore necessary to take the buffering into account.

Culture media typically contain a large number of different proteins, salts, and other nutrients, which will interact with each other in complex ways under applied pH changes. We therefore make no attempt to model the buffering effect, and instead appeal to experimental results. Fig. A1 shows data from two titrations of lactic acid into a typical culture medium. From this data, we see that the concentration of lactic acid that results in a pH drop of 0.5 is roughly $0.4\,\mathrm{mol\,m^{-3}}$. We use this for the value of $c_i^\dagger$ in Section 7.

Appendix B. Consistency of the approximations used in Section 4

In this appendix, we check the consistency of the various approximations used in Section 4 to model the flow in the fibre. These approximations simplified the equations in the core and wall. We check their validity by comparing the sizes of the neglected terms to those retained.

To obtain the viscous lubrication approximation (37)–(39) in the fibre core, we assumed that the appropriate Reynolds number is small, and that the radial pressure variation Δp_r required to drive the radial flow is small compared with the axial pressure variation Δp_s. The Reynolds number is estimated by comparing the steady inertia term with the viscous term. We find that

$$Re_c = \frac{\rho w_c^2/a}{\mu w_c/b_c^2} \sim \frac{\rho Q_f}{\mu a} = \frac{\rho Q_-}{\mu a}\frac{\mathscr{Q}}{N} \approx \frac{20\mathscr{Q}}{N} \lesssim O(1). \tag{B.1}$$

While this may not be formally small, low-Reynolds-number approximations are generally found to be acceptable even at $O(1)$ Reynolds numbers. Moreover, in the $\alpha^2 \ll 1$ regime of primary interest here, $O(1)$ errors in the viscous pressure drop along the fibre will not affect the pressure difference across the wall, and so the emitted flux will be unchanged.

The pressure variations Δp_r and Δp_s are estimated from the viscous drag due to the velocity components. We therefore have

$$\frac{\Delta p_s}{L} \sim \mu\frac{w_c}{b_c^2} \sim \frac{\mu Q_f}{b_c^4}, \quad \frac{\Delta p_r}{b_c} \sim \mu\frac{u_c}{b_c^2} \sim \frac{\mu Q_f}{ab_c^3}, \tag{B.2}$$

and hence

$$\frac{\Delta p_r}{\Delta p_s} \sim \frac{b_c^2}{\ell a^2} \sim \varepsilon^2. \tag{B.3}$$

We have already assumed that $\varepsilon \ll 1$, so the approximation is justified.

Secondly, when forming equations (46)–(47) for the flow in the wall, we assumed that the axial flow made no contribution to the continuity equation, and so could be neglected. Knowing that the axial pressure variations in the wall are tied to $p_c(s)$ from (30b), we can now estimate

$$\frac{\partial w_w}{\partial s} \lesssim \frac{\bar{k}_w}{\mu}\frac{\partial^2 p_c}{\partial s^2} \sim \frac{Q_f}{a^3}\frac{\partial^2 P_c}{\partial \zeta^2} \sim \frac{\alpha^2 Q_f}{a^3} \sim \frac{Q_f \bar{k}_w}{\varepsilon^4 a^5}. \tag{B.4}$$

This must be small compared with $u_w/b_c \sim Q_f/(\varepsilon^2 a^3)$. Hence we require

$$\bar{k}_w \ll \varepsilon^2 a^2 = b_c^2, \tag{B.5}$$

a condition that we had already noted.

References

Abousleiman, R.I., Sikavitsas, V.I., 2006. Bioreactors for tissues of the musculoskeletal system. Adv. Exp. Med. Biol. 585, 243–259.
Bailey, C., et al., 2006. Optimisation of fluid distribution inside a porous construct. In: Proceedings of the 6th Mathematics in Medicine Study Group. University of Nottingham.
Bancroft, G., Sikavitsas, V., van den Dolder, J., Sheffield, T., Ambrose, C., Jansen, J., Mikos, A., 2002. Fluid flow increases mineralized matrix deposition in 3D perfusion culture of marrow stromal osteoblasts in a dose-dependent manner. Proc. Natl. Acad. Sci. USA 99 (20), 12600–12605.
Batchelor, G.K., 1967. An Introduction to Fluid Dynamics. Cambridge University Press, Cambridge.
Bear, J., 1988. Dynamics of Fluids in Porous Media. Dover.
Boschetti, F., Raimondo, M.T., Migliavacca, F., Dubini, G., 2006. Prediction of the micro-fluid dynamic environment imposed to three-dimensional engineered cell systems in bioreactors. J. Biomech. 39, 418–425.
Cartmell, S.H., Porter, B.D., Garcia, A.J., Guldberg, R.E., 2003. Effects of medium perfusion rate on cell-seeded three-dimensional bone constructs *in vitro*. Tissue Eng. 9 (6), 1197–1203.
Cartmell, S.H., Gittings, J.P., Turner, I.G., Chaudhuri, J.B., Ellis, M.J., Waters, S.L., Cummings, L.J., Kuiper, N.J., Michael, V., 2007. Bioreactor design for

osteochondral tissue. In: American Society of Bone and Mineral Research, 29th Annual Meeting Abstracts Supplement. J. Bone Miner. Res. 22S1, S162.
Cimetta, E., Flaibani, M., Mella, M., Serena, E., Boldrin, L., De Coppi, P., Elvassore, N., 2007. Enhancement of viability of muscle precursor cells on 3D scaffold in a perfusion bioreactor. Int. J. Artif. Organs 30 (5), 415–428.
Cogan, N.G., Keener, J.P., 2004. The role of the biofilm matrix in structural development. Math. Med. Biol. 21, 147–166.
Cummings, L.J., Waters, S.L., 2007. Tissue growth in a rotating bioreactor. Part II: flow and nutrient transport problems. Math. Med. Biol. 24, 169–208.
Ellis, M.J., Chaudhuri, J.B., 2007. Poly(lactic-co-glycolic acid) hollow fibre membranes for use as a tissue engineering scaffold. Biotech. Bioeng. 96 (1), 177–187.
Galban, C.J., Locke, B.R., 1997. Analysis of cell growth in a polymer scaffold using a moving boundary approach. Biotech. Bioeng. 56 (4), 422–432.
Galban, C.J., Locke, B.R., 1999. Effects of spatial variations of cells and nutrient and product concentrations coupled with product inhibition on cell growth in a polymer scaffold. Biotech. Bioeng. 64 (6), 633–643.
Gittings, J.P., Turner, I.G., Miles, A.W., 2005. Calcium phosphate open porous scaffold bioceramics. Key Eng. Mat. 284–286, 349–354.
Glowacki, J., Mizuno, S., Greenberger, J.S., 1998. Perfusion enhances functions of bone marrow stromal cells in three-dimensional culture. Cell Transp. 7 (3), 319–326.
Goldstein, A., Juarez, T., Helmke, C., Gustin, M., Mikos, A., 2001. Effect of convection on osteoblastic cell growth and function in biodegradable polymer foam scaffolds. Biomaterials 22 (11), 1279–1288.
Haddock, S.M., Debes, J.C., Nauman, E.A., Fong, K.E., Arramon, Y.P., Keaveny, T.M., 1999. Structure-function relationships for coralline hydroxyapatite bone substitute. J. Biomed. Mater. Res. 47 (1), 71–78.
Humphrey, J.D., 2003. Continuum biomechanics of soft biological tissues. Proc. R. Soc. London A 459 (1), 3–46.
Invitrogen, 2008. Dulbecco's Modified Eagle Medium (D-MEM) (1X) #22320022. Media formulations, Invitrogen.
Kim, S.S., Penkala, R., Abrahimi, P., 2007. A perfusion bioreactor for intestinal tissue engineering. J. Surg. Res. 142 (2), 327–331.
Knobloch, T.J., Madhavan, S., Nam, J., Agarwal, S.J., Agarwal, S., 2008. Regulation of chondrocytic gene expression by biomechanical signals. Crit. Rev. Eukaryotic Gene Exp. 18 (2), 139–150.
Komarova, S.V., Ataullakhanov, F.I., Globus, R.K., 2000. Bioenergetics and mitochondrial transmembrane potential during differentiation of cultured osteoblasts. Am. J. Physiol. Cell Physiol. 279, C1220–C1229.
Koponen, A., Kataja, M., Timonen, J., 1996. Tortuous flow in porous media. Phys. Rev. E 54 (1), 406–410.
Lasseux, D., Ahmadi, A., Cleis, X., Garnier, J., 2004. A macroscopic model for species transport during *in vitro* tissue growth obtained by the volume averaging method. Chem. Eng. Sci. 59 (10), 1949–1964.
Lemon, G., King, J.R., Byrne, H.M., Jensen, O.E., Shakesheff, K.M., 2006. Mathematical modelling of engineered tissue growth using a multiphase porous flow mixture theory. J. Math. Biol. 52 (5), 571–594.
Lide, D.R. (Ed.), 2007. CRC Handbook of Chemistry and Physics, 87th ed. CRC.
MacArthur, B.D., Please, C.P., Taylor, M., Oreffo, R.O.C., 2004. Mathematical modelling of skeletal repair. Biochem. Biophys. Res. Commun. 313, 825–833.
Martin, I., Wendt, D., Heberer, M., 2004. The role of bioreactors in tissue engineering. Trends Biotechnol. 22 (2).
Michael, V., Gittings, J.P., Turner, I.G., Chaudhuri, J.B., Ellis, M.J., Waters, S.L., Cummings, L.J., Goodstone, N.J., Cartmell, S.H., 2007. Co-culture bioreactor design for skeletal tissue engineering. In: TERMIS-EU Meeting Abstracts. Tissue Eng. 13(7), 1657–1658.
Morgan, S.M., Tilley, S., Perera, S., Ellis, M.J., Kanczler, J., Chaudhuri, J.B., Oreffo, R.O.C., 2007. Expansion of human bone marrow stromal cells on poly-(dl-lactide-co-glycolide) (P(DL)LGA) hollow fibres designed for use in skeletal tissue engineering. Biomaterials 28 (35), 5332–5343.
Nehring, D., Adamietz, P., Meenen, N.M., Pörtner, R., 1999. Perfusion cultures and modelling of oxygen uptake with three-dimensional chondrocyte pellets. Biotechnol. Tech. 13 (10), 701–706.
Ockendon, H., Ockendon, J.R., 1995. Viscous Flow. Cambridge University Press, Cambridge.
O'Dea, R.D., Waters, S.L., Byrne, H.M., 2008. A two-fluid model for tissue growth within a dynamic flow environment. Eur. J. Appl. Math. 19, 607–634.
Peterson, L., Minas, T., Brittberg, M., Nilsson, A., Sjögren-Jansson, E., Lindahl, A., 2000. Two to nine year outcome after autologous chondrocyte transplantation of the knee. Clin. Orthop. Relat. Res. 374, 212–234.
Porter, B., Zauel, R., Stockman, H., Guldberg, R., Fyhrie, D., 2005. 3D computational modeling of media flow through scaffolds in a perfusion bioreactor. J. Biomech. 38 (3), 543–549.
Ribeiro, A.C.F., Lobo, V.M.M., Leaist, D.G., Natividade, J.J.S., Veríssimo, L.P., Barros, M.C.F., Cabral, A.M.T.D.P.V., 2005. Binary diffusion coefficients for aqueous solutions of lactic acid. J. Soltn. Chem. 34, 1009–1016.
Rubin, J., Rubin, C., Jacobs, C.R., 2006. Molecular pathways mediating mechanical signaling in bone. Gene 367, 1–16.
Sengers, B.G., Oomens, C.W.J., Baaijens, F.P.T., 2004. An integrated finite-element approach to mechanics, transport and biosynthesis in tissue engineering. J. Biomech. Eng. 126 (1), 82–91.
Tromans, D., 1998. Temperature and pressure dependent solubility of oxygen in water: a thermodynamic analysis. Hydrometallurgy 48 (3), 327–342.
Waters, S.L., Cummings, L.J., Shakesheff, K.M., Rose, F.R.A.J., 2006. Tissue growth in a rotating bioreactor. Part I: mechanical stability. Math. Med. Biol. 23, 311–337.
Yu, B.-M., Li, J.-H., 2004. A geometry model for tortuosity of flow path in porous media. Chin. Phys. Lett. 21 (8), 1569–1571.